PCCP

Composition, Crystallography, and Oxygen Vacancy Ordering Impacts on the Oxygen Ion Conductivity of Lanthanum Strontium Ferrite

Journal:	*Physical Chemistry Chemical Physics*
Manuscript ID	CP-ART-01-2020-000206.R2
Article Type:	Paper
Date Submitted by the Author:	16-Apr-2020
Complete List of Authors:	Das, Tridip; Michigan State University, Department of Chemical Engineering and Materials Science; Michigan State University Nicholas, Jason; Michigan State University, Chemical Engineering and Materials Science Department Qi, Yue; Michigan State University, Department of Chemical Engineering and Materials Science

SCHOLARONE™
Manuscripts

Composition, Crystallography, and Oxygen Vacancy Ordering Impacts on the Oxygen Ion Conductivity of Lanthanum Strontium Ferrite

Tridip Das, Jason D. Nicholas, and Yue Qi*

Chemical Engineering & Materials Science Department, Michigan State University, 428 South

Shaw Lane, 2527 Engineering Building, East Lansing, MI 48824, USA

ABSTRACT

This work presents a comprehensive computational study showing how aliovalent doping, crystal structure, and oxygen vacancy interactions impact the oxygen vacancy conductivity of lanthanum strontium ferrite (LSF) as a function of temperature in air. First, density functional theory (DFT) calculations were performed to obtain the oxygen vacancy migration barriers and understand the oxidation state changes on neighboring Fe atoms during oxygen vacancy migration. The oxygen migration barrier energy and the corresponding diffusion coefficient were then combined with previously determined mobile oxygen vacancy concentrations to predict the overall oxygen vacancy conductivity and compare it with experimentally measured values. More importantly, the impact of phase changes, the La/Sr ratio, and the oxygen non-stoichiometry on the mobile oxygen vacancy concentration, diffusivity, and conductivity were analyzed. It was found that stabilizing rhombohedral LSF or cubic SFO (through doping or other means), such that oxygen-vacancy-ordering-induced phase transitions are prevented, leads to high oxygen conductivity under solid oxide fuel cell operating conditions.

*Corresponding author: yueqi@egr.msu.edu

I.   INTRODUCTION

Mixed Ionic Electronic Conducting (MIEC) oxides with high electronic conductivity and high oxygen ion conductivity are used in a variety of high-tech devices including oxygen sensors,[1] gas separation membranes,[2] catalytic converters,[3] Solid Oxide Fuel Cells (SOFCs),[4] Solid Oxide Electrolysis Cells,[5] memristors,[6] electrochromic displays,[7] etc. Although MIEC oxides come in fluorite,[8] Ruddlesden-Popper,[9] double perovskite,[10] and a variety of other crystal structures, perovskite-structured MIEC oxides have received the most attention in the literature due to their favorable properties, tolerance to manipulation by doping, and relative stability.[4] Of these, lanthanum strontium ferrite (pure and especially cobalt doped lanthanum strontium ferrite[11]) is one of the most experimentally well-studied. In these MIEC oxides, many coupled factors, including the aliovalent doping level, the charge state of multivalent lattice ions, the crystal structure, the oxygen non-stoichiometry, the temperature, and the strain imposed on the structure control oxygen vacancy formation and migration, and thus the overall oxygen conductivity.[9] Therefore, the present paper focuses on detailing the underlying relationships among these factors and their impact on the oxygen vacancy conductivity of lanthanum strontium ferrite as a function of temperature.

As just mentioned, many factors influence oxygen vacancy formation and migration in lanthanum strontium ferrite, $La_{1-x}Sr_xFeO_{3-\delta}$ (LSF). These factors include the La/Sr ratio, the temperature, the crystal structure, the charge distribution on neighboring multivalent Fe atoms, the oxygen non-stoichiometry (δ), and the interactions between oxygen vacancies at higher δ. [12–14] These factors are intertwined, as shown in the combined phase diagram for LSF in Figure 1. For instance, below 1000 ºC LSF changes from orthorhombic to rhombohedral to eventually cubic, as the La/Sr ratio decreases from one to zero. Similarly, the LSF solid solution end member $SrFeO_3$

2

(SFO) experiences cubic, tetragonal, orthorhombic, and brownmillerite phase changes with increasing temperature and increasing δ.

Obtaining high, stable oxygen ion transport below ~650 ℃ in LSF and related MIEC compounds has been desired, but challenging, for SOFC applications.[14–18] Interestingly, the oxygen ion conductivity of LSF does not exponentially increase with temperature due to phase changes and oxygen vacancy interactions at higher vacancy concentration.[19–21] Further, attempts to improve the performance of these MIEC compounds via doping, lattice strain engineering, or other extrinsic means has been complicated by a lack of understanding of how these intertwined factors regulate MIEC oxygen ion conductivity.

The ionic conductivity depends on both the formation and the diffusion of ionic defects.[22,23] In MIEC perovskite materials like LSF, the oxygen ions move via a vacancy hopping mechanism,[24] and the oxygen ion conductivity (σ) can be calculated using the relation:

$$\sigma = \frac{Z^2 e^2 c D}{k_B T}$$

[1],

where c is the mobile oxygen vacancy concentration, Z is the charge on the oxygen ion as a multiple of e (the charge of an electron), and D is the oxygen vacancy diffusivity.[22,23] Therefore, the 1) oxygen vacancy formation energy and 2) oxygen vacancy migration energy barrier are the major factors controlling the oxygen vacancy concentration and diffusivity, respectively.

Previous LSF computational studies have shown that the oxygen vacancy formation energy varies by ~3 eV as the La/Sr ratio is decreased from one to zero.[25] Also, a significant variation (~2.5 eV) was observed in the SFO oxygen vacancy formation energy with temperature due to the multiple SFO phase changes shown in Figure 1.[19] In addition, previous experimental and computational studies of oxygen vacancy migration in LSF have suggested that A-site doping

has a negligible effect on the LSF oxygen migration barriers.[26–29] Specifically, these prior density functional theory (DFT) studies[29,30] have produced results consistent with the statement from Mastrikov *et al.*[26,29] that "In $(La,Sr)(Mn,Fe,Co)O_{3-\delta}$ perovskites, the oxygen vacancy diffusion coefficients were experimentally found to be almost independent of the cation composition, with a typical migration barrier of ≈ 0.8 eV". However, these earlier DFT studies were not completed over a broad range of LSF La/Sr ratios, crystallographic phases, and/or oxygen non-stoichiometry levels. In addition, these previous DFT oxygen vacancy diffusivity calculations also assumed dilute oxygen vacancies,[24,29] even though this is not always the case. The work of. Das *et al.*,[25] recently showed that the critical δ threshold, above which oxygen vacancies are interacting, increases with La/Sr ratio and decreases with the oxygen vacancy polaron size. This critical δ threshold is ~0.05, ~0.1, ~0.25, >0.25, in cubic SFO, cubic LSF55, rhombohedral LSF55, and LFO, respectively. Since the experimentally observed typical δ at the SOFC operating temperature is ~ 0.1 for LSF55 and ~0.3 for SFO, [31,32] vacancy interactions should be considered in the high temperature cubic SFO and cubic LSF55 phases.[25]

Das *et al.*[25] overcame several computational challenges to predict the overall oxygen vacancy non-stoichiometry and the mobile vacancy site fraction in LSF as a function of La/Sr ratio, temperature, and crystallographic phase. First, the interacting oxygen vacancies were shown to lead to an increasing vacancy formation energy with vacancy concentration, necessitating the development of a new computational model to predict the oxygen-vacancy-concentration-dependent non-stoichiometry in both dilute and non-dilute cases.[19] Second, since the mobile oxygen vacancy concentration, c in Equation 1, is not necessarily equal to the overall oxygen non-stoichiometry (δ) due to the formation of structural oxygen vacancies, c was related to the mobile oxygen vacancy site fraction, X via the Equation:

$$c = (3 - \delta^0)X/V_u \tag{2},$$

where V_u is the volume per formula unit and δ^0 is the nonstoichiometry lost due to oxygen vacancy ordering included phase transformations that reduce the total number of lattice oxygen sites. Equation [2] holds for phases both with and without oxygen vacancy ordering. For phases without vacancy ordering, $\delta^0 = 0$; thus, $\delta = 3X$ and $c = \delta/V_u$. For the vacancy-ordered-phases in this study, $\delta^0 = 0.125$ in tetragonal SFO, $\delta^0 = 0.25$ in orthorhombic SFO, and $\delta^0 = 0.25$ in brownmillerite SFO.

The present work focused on how the oxygen vacancy diffusivity and ionic conductivity in LSF vary with La/Sr ratio, temperature, and oxygen nonstoichiometry in order to determine the LSF composition with the maximum ionic conductivity under SOFC operating conditions. This was achieved by using the DFT calculation methods described in Section 2 to compute the oxygen ion migration barriers at different representative oxygen vacancy concentrations in orthorhombic $LaFeO_{3-\delta}$ (LFO), rhombohedral $La_{0.5}Sr_{0.5}FeO_{3-\delta}$ (LSF55), cubic LSF55, cubic $SrFeO_{3-\delta}$ (SFO), tetragonal SFO, and orthorhombic SFO. Due to the extremely high oxygen vacancy formation energy of ~3 eV in brownmillerite SFO that makes it impractical for most SOFC applications, its diffusion barrier was not analyzed here. The previously predicted mobile oxygen vacancy concentration, c, from Das $et\ al.$[19]. was then combined with the newly predicted oxygen vacancy diffusivity D in this study to calculate the LSF oxygen ionic conductivity as a function of temperature and phase, in air. These results were then used to explain the phase-transition-induced loss of oxygen conductivity observed experimentally.[33,34]

II.   COMPUTATIONAL DETAILS

The oxygen migration barriers following all possible oxygen vacancy migration pathways in cubic, tetragonal, and orthorhombic SFO, rhombohedral LSF55, and orthorhombic LFO were calculated and compared at 0 K. All calculations were performed with VASP (Vienna *Ab initio* Simulation Package), a planewave-based DFT method. Projector-augmented-wave (PAW) potentials with valence configurations of $5s^25p^65d^16s^2$ for La, $4s^24p^65s^2$ for Sr, $3d^74s^1$ for Fe, and $2s^22p^4$ for O were used to describe the valence electrons. The generalized gradient approximation (GGA) functional along with Perdew, Burke, and Ernzerhof (PBE) parameters were used to describe the exchange-correlation potentials of the constituting elements. Fe was treated with the GGA+U method with a $U_{eff} = 3$, that have been shown previously to describe the lattice parameters and the charge states of Fe in both $LaFeO_3$ and $SrFeO_3$ reasonably well.[25] Spin-polarized calculations were performed and the magnetic moment on each Fe was calculated by spherical integration. From convergence studies, it was determined that a *k*-spacing of 0.2 Å^{-1} and a cutoff energy of 500 eV were sufficient. The accuracy for each electronic calculation was within 1 μeV and the ionic relaxations were performed until the Hellmann-Feynman force on each atom reached the order of 10 meV/ Å.[35]

The migration energy was calculated using the Climb Image Nudge Elastic Band (CINEB) method[36] which also provided the transition state structure at the saddle point.[37] The diffusion path was set initially along the Fe-O octahedral edges and three images between the start and end points were used for each path. Specifically, the CINEB method found the image structure with the minimum energy path (MEP)[38,39] and the maximum value of the potential energy along that path was used to determine the diffusion activation energy (barrier) using the Equation:

$$D = \frac{1}{n}d^2\nu\exp\left(-\frac{E_m}{k_BT}\right) \qquad [3]$$

where, E_m is the CINEB calculated oxygen vacancy migration barrier, d is the vacancy migration distance, v is the jump frequency (which was assumed to be 10^{13} Hz for solid state diffusion[40]), n is the number of possible jump directions with the minimum energy barrier. For isotropic diffusion in a cubic lattice, $n=6$. For anisotropic diffusion, multiple vacancy migration pathways were evaluated and only the lowest diffusion path was counted. Thus, n is the number of possible jump directions with the minimum energy barrier and d represents the jump distance for that minimum energy barrier.

Table 1 summarizes the atomic structures used in the simulation. More detailed discussions about these structures and properties can be found in previous oxygen vacancy formation studies.[19,25] All vacancies were assumed to be charge neutral. Lastly, the changes in the neighboring Fe oxidation states during oxygen vacancy migration were determined by interpreting the magnetic moments of the neighboring Fe atoms following the procedures described in Das *et al.*[19]

III.   RESULTS

3.1 Oxygen Vacancy Migration in LaFeO_{3-δ}

Figure 2(a) shows the oxygen migration pathway in LFO, highlighted with pink atoms. The lattice distortion shown in Figure 2(a) corresponds to the transition state lattice distortion. The calculated migration barrier in two simulations cells with two different LFO oxygen nonstoichiometries ($\delta = 0.06$ and 0.25), shown in Figure 2(b), possess the same migration energy barrier of 0.89 eV. This confirms that even at high oxygen nonstoichiometry concentrations ($\delta = 0.25$), oxygen vacancies do not interact in LFO. Further, this calculated oxygen vacancy migration barrier in LFO is comparable to the experimentally observed oxygen migration barrier of 0.77 eV

obtained in oxygen tracer diffusion experiments[26] and the 1.1 eV obtained in conductivity relaxation experiments.[41]

Figure 2(c) shows the small polaron (dashed purple line) generated by neutral oxygen vacancy formation (i.e. the oxygen vacancy and the two electrons left behind by its formation) in LFO. Based on the magnetic-moment-interpreted oxidation state of the Fe atoms, Das *et al*,[25] found that the two Fe atoms connected to the oxygen vacancy site became 2+, while the other Fe atoms in the lattice remained 3+ (as in stoichiometric LFO). Thus, the small polaron in LFO is elongated along a length of ~4.0 Å. Figure 2(d) shows how the magnetic moment changes on the four oxygen-vacancy-neighboring Fe atoms (labeled in Figure 2(a)) during oxygen vacancy migration. This calculation shows that the magnetic-moment-interpreted oxidation state[19] of the second nearest neighboring Fe (Fe4) remains constant at 3+ during oxygen vacancy migration. This finding is consistent with the small polaron size shown in Figure 2(c). Furthermore, it can be noticed that when an oxygen atom moves from one equilibrium site ($\zeta = 0$) to another equilibrium site ($\zeta = 1$), the Fe2 atom reduces its charge from Fe^{3+} to Fe^{2+} and Fe3 changes its charge from Fe^{2+} to Fe^{3+}, as the oxygen vacancy moves away from Fe3 to Fe2 along the opposite direction as the path of oxygen atom. It is interesting to note that at the transition state, both Fe2 and Fe3 are close to $Fe^{2.3+}$ due to the partial distribution of the two electrons among Fe1, Fe2 and Fe3. The magnetic moment on Fe1 drops at the transition state, suggesting that Fe1 becomes a low-spin $Fe^{2.3+}$ at the transition state. This is further confirmed by a Projected Density of States (PDOS) analysis. Low spin Fe in perovskite structure is rare, its occurrence at the transition state with large local structure distortion, might be due to weak Jahn-Teller effect with low spin Fe. After the oxygen atom completes its move to $\zeta = 1$, the magnetic moment on Fe1 (i.e. the oxygen-vacancy-adjacent Fe) returns to Fe^{2+}.

3.2 Oxygen Vacancy Migration in $La_{0.5}Sr_{0.5}FeO_{3-\delta}$

Figures 3(a) and 4(a) show the oxygen migration pathways in rhombohedral and cubic LSF55, respectively. Similar to the structures used in previous oxygen vacancy formation studies,[25] ordered LSF55 phases were assumed here in which an alternate layer of La-O and Sr-O was separated by the Fe-containing layer, as shown in Figure 3(c) and 4(c). This is representative, as a single phase behavior of LSF55 was observed experimentally and the extensive site ordering of La/Sr simulated by Ritzmann *et al.* [14] revealed a weak dependence of the oxygen vacancy formation energy on the La/Sr site configuration. The calculated oxygen migration barriers are shown in Figure 3(b) and 4(b) for rhombohedral and cubic LSF55. The calculated migration barrier in rhombohedral LSF55 is 0.45 eV for both dilute and interacting vacancies (at $\delta = 0.04$ and 0.17). As discussed previously, it is not computationally possible to obtain a stable cubic LSF55 structure with very low oxygen vacancy concentration,[25] as the local structure prefers tilted octahedra around each oxygen vacancy. In this study, for cubic LSF55, the calculated oxygen migration barrier is 0.70 eV at $\delta = 0.13$. Due to the lattice distortions in cubic LSF55, the two Fe-O octahedra sharing the diffusing oxygen tilt dramatically and locally transform into a "rhombohedral LSF55"-like structure, resulting a significant decrease in the total energy at $\zeta = 0.25$ and $\zeta = 0.75$. This results in a "trapped state" in the vacancy migration pathway and the diffusion barrier is from this trapped state to the saddle point transition state. These results explain why the rhombohedral to cubic LSF55 phase change has less of an impact on the oxygen migration barrier (it only differs by ~0.25 eV) than the on oxygen vacancy formation energy (it differs by ~0.5 eV).[25]

Figure 3(c) and 4(c) show that the polaron shape (dashed purple line) around an oxygen vacancy (indicated by the black dot) is asymmetric in rhombohedral LSF55 but symmetric in the cubic LSF55. In Figures 3(d) and 4(d), the changes in the magnetic moment of the oxygen-vacancy-neighboring Fe atoms are shown in rhombohedral and cubic LSF55, respectively. The oxygen-vacancy-adjacent Fe1 maintains the same oxidation state before and after oxygen vacancy migration, but not at the transition state, in both rhombohedral and cubic LSF55. In rhombohedral LSF55, magnetic-moment-interpreted charge transfer shows that the oxidation state on Fe4 (a second nearest neighbor to the oxygen vacancy) is slightly oxidized as the oxygen vacancy passes by, which is presumably due to the asymmetric polaron shape. In contrast, in cubic LSF55 where the polaron shape is symmetrical, the magnetic-moment-interpreted charge on Fe4 does not change as the oxygen vacancy passes by. After the migration of the oxygen vacancy from the Fe3-adjacent site to the Fe2-adjacent site, the magnetic moments indicate that the oxidation states on Fe2 and Fe3 exchange in cubic LSF55. The exchange occurs at the transition state. However, the magnetic moments of Fe2 and Fe3 do not exchange simply in rhombohedral LSF55, due to the anisotropic shape of the polaron.[25] Figure 4(d) shows a sudden dip in the magnetic moment or a increase in Fe oxidation state due to the low spin state configuration associated with a weak Jahn–Teller distortion observed in the "trapped state" in the migration path. The larger change of the magnetic moment and the charge state on Fe is consistent with the higher migration energy barrier in cubic LSF55 compared to rhombohedral LSF55.

3.3 Oxygen Vacancy Migration in SrFeO$_{3-\delta}$

Figure 5(a) shows the oxygen migration pathway (pink atoms) in cubic SFO. As shown in Figure 5(b), the calculated oxygen migration barriers in cubic SFO are 0.58, 0.62 and 1.07 eV at

δ = 0.04, 0.12, and 0.5 respectively. These results show that the effect of oxygen non-stoichiometry on the oxygen vacancy migration barrier is insignificant (<0.05 eV) below a critical non-stoichiometry, above which oxygen vacancies strongly interact (between δ=0.12 and δ = 0.5). Since the oxygen vacancy nonstoichiometry is less than ~0.125 in cubic SFO until it transforms to the tetragonal phase, below this concentration, the migration energy barrier is ~0.6 eV and does not change with δ. Figure 5(c) shows the large pancake-shaped polaron[19] generated by neutral oxygen vacancy formation in cubic SFO. Note, the cubic phase with δ = 0.5 is not a stable phase, the data is provided as an example of the impact high concentrations of oxygen vacancies have on cubic SFO. Figure 5(d) shows the magnetic moment change on the neighboring Fe atoms during oxygen vacancy migration. Initially (at ζ = 0), the oxygen vacancy is between Fe1 and Fe3. Therefore, the oxidation state on square pyramidal-Fe1 and Fe3 are the same (~4.1+) corresponding to the vacancy adjacent or nearest neighboring Fe atoms. The magnetic-moment-interpreted charge of Fe2 and Fe4 are also the same (~3.8+) corresponding to the oxygen vacancy second nearest neighboring Fe atoms (Figure 5(c)). After an oxygen vacancy moves to the site between Fe1 and Fe2 (ζ = 1), the magnetic-moment-interpreted charge on Fe2 increases to 4.1+ due to the square pyramidal coordination and the second-nearest-neighboring Fe3 and Fe4 have an oxidation state of 3.8+ due to the octahedral coordination. This indicates that the oxidation states of Fe2 and Fe3 have exchanged due to oxygen vacancy migration. According to Figure 5(d), the interchange occurs at the transition state. At the transition state, the magnetic moment on the vacancy adjacent Fe1 goes through a minimum indicating that the Fe oxidation state is increased at the transition state, which is consistent with the excess electrons being pushed to the second nearest neighboring Fe4. Fe1 maintains the same oxidation state (~4.1+) before and after oxygen vacancy migration due to its square pyramidal coordination with neighboring oxygen atoms.

Overall, Figure 5(d) shows that the extent of the magnetic moment/Fe oxidation state change on the oxygen-vacancy-neighboring Fe ($\sim0.3\mu_B$) is not as large as it is for LFO ($\sim1.3\mu_B$) due to the more distributed electrons or the larger polaron size of $\sim7.8 \times 3.9$ Å, shown in Figure 5(c).

The presence of multiple nonequivalent oxygen sites in tetragonal and orthorhombic strontium ferrites leads to long hopping distances and many different migration paths, as shown in Figures 6 and 7. Hopping to the equivalent site with the lowest oxygen vacancy formation energy requires a path through multiple oxygen sites. Following previous work,[42] here the Wyckoff positions of the oxygen atoms in the perfect lattice were used to denote different migration paths. Figure 6 (a) shows three paths in tetragonal SFO with $\delta = 0.188$ and $\delta^0 = 0.125$ (Note, δ^0 corresponds to the perfect tetragonal SFO phase of $SrFeO_{2.875}$). There are six non-equivalent oxygen sites, and the most energetically favorable oxygen vacancy site is 4c. Path $\vec{a}, \vec{b}$ and $\vec{c}$ follows 4c → 16k → 8h → 16k → 4c, 4c → 16k → 16m → 16k → 4c; and 4c → 16k → 4c, respectively. Since the three different migration paths have almost the same oxygen vacancy migration barrier of ~0.71 eV, the diffusion in tetragonal SFO is isotropic in nature. Figure 7(a) shows the oxygen migration pathways in ink atoms in orthorhombic SFO with $\delta = 0.312$ and $\delta^0 = 0.250$ (Note, Note, δ^0 corresponds to the perfect orthorhombic SFO structure of $SrFeO_{2.75}$). There are three non-equivalent oxygen sites, and the most energetically favorable oxygen vacancy site is 2b. Path $\vec{a}, \vec{b}$ and $\vec{c}$ follows 2b → 16r → 16r → 2b; 2b → 16r → 4j → 16r → 2b; and 2b → 16r → 16r → 2b, respectively. These diffusion paths go through oxygen sites with elevated oxygen vacancy formation energy, as shown in Fig 7(c), resulting in a lowest migration barrier that is 1.17 eV in orthorhombic SFO and slightly anisotropic in nature.

3.4 Oxygen Ionic Conductivity in $La_{1-x}Sr_xFeO_{3-\delta}$ as a Function of Temperature (in Air)

Figure 8 shows the concentration, diffusivity, and ionic conductivity of LFO, LSF55, and SFO. As shown in Figure 1, the experimental LSF phase diagram contains several phase transformations.[43] To facilitate a direct comparison with experiments, the "LSF55 (combined)" data includes the rhombohedral to cubic phase transformation at $250 \pm 50°C$.[43] In contrast, to illustrate the impact of phase changes on the ionic conductivity, individual phases, such as "Cubic SFO" and "Rhomb LSF55", were calculated, for comparison, by ignoring the phase changes. " HT SFO" includes the high temperature phases, such as the tetragonal, orthorhombic and brownmillerite SFO phases, which were plotted over their specific stable temperature ranges. The ionic conductivity for LFO was too low to be shown in Figure 7(c) due to its very high oxygen vacancy formation energy.

Figure 8(a) shows the computed mobile oxygen vacancy concentration, c, in different phases of LSF. Due to a very high oxygen vacancy formation energy of ~3.5 eV,[25] the mobile oxygen vacancy concentration in LFO (which is orthorhombic over the entire temperature range) is relatively low. In contrast, the mobile oxygen vacancy concentration in LSF55 is higher and shows an order of magnitude drop around 250°C due to the rhombohedral to cubic phase transition in the bulk structure.[43] The increase in the mobile oxygen vacancy concentration with temperature slows down in (cubic) LSF55 above ~750°C due to the onset of oxygen vacancy interactions. Cubic SFO has a high oxygen vacancy concentration from 0 to 1000°C, but it does not increase exponentially with temperature due to the strong vacancy interactions that led to an increase in oxygen vacancy formation energy with increasing oxygen vacancy concentration.[19] However, the mobile oxygen vacancy concentration in the high temperature SFO phases (tetragonal, orthorhombic, brownmillerite) fluctuates with temperature due to oxygen vacancy ordered phase transitions which cause a loss in the mobile oxygen vacancy concentration due to vacancy site

ordering (Equation 2). Once brownmillerite SFO is formed at high temperature (~700°C), the vacancy concentration is drastically reduced by 8 orders of magnitude due to the high oxygen vacancy formation energy of ~3 eV. As a result, the oxygen vacancy concentration in brownmillerite SFO becomes comparable to the oxygen vacancy concentration in LFO. A maximum in the oxygen vacancy concentration can be observed in orthorhombic SFO at ~ 650°C in air.

Figure 8(b) shows the oxygen diffusivity in different phases of LSF. The oxygen diffusivity in LFO is lower than the other LSF compositions below ~ 750°C. The diffusivity of oxygen in tetragonal and orthorhombic SFO is also lower than cubic SFO due to the higher migration barriers shown in Figures 5, 6, and 7, respectively. The oxygen vacancy migration barrier increases from 0.7 eV in tetragonal SFO to 1.17 eV in orthorhombic SFO due to oxygen vacancy ordering. Although cubic SFO is not stable at high temperature range, it is still interesting to show the effect of oxygen vacancy interactions on its mobility. When the oxygen vacancies' nonstoichiometry is above 0.125, they start to interact. The migration barrier was extrapolated linearly from 0.62 eV at $\delta = 0.12$ (~300°C) to 1.07 eV at $\delta = 0.5$ (~800°C) (based on Fig 5), and the corresponding oxygen diffusivity displays less than exponential growth with temperature. Rhombohedral LSF55 shows the highest oxygen ionic diffusivity in the LSF family at low temperatures. However, the LSF55 oxygen vacancy diffusivity drops above 250°C, due to rhombohedral to cubic phase transition and the higher oxygen vacancy migration barrier in cubic LSF55 (0.7 eV) compared to rhombohedral LSF55 (0.45 eV).

Figure 8(c) shows the ionic conductivity of different LSF phases. It clearly illustrates that LSF55 possesses an ionic conductivity that is higher than LFO or SFO at or above 800°C in air. This is consistent with the work of Patrakeev et al.[44] who have experimentally shown that LSF55

possesses the highest oxygen ionic conductivity within the LSF family at 950°C in air. The calculated ionic conductivity for LSF55 at 950°C is 0.40 S/cm and is comparable to experimentally measured value of 0.5 S/cm at the same temperature.[44]

The dotted "Rhomb LSF55" line represents a hypothetical rhombohedral LSF55 phase (as rhombohedral LSF55 transforms in real-life to cubic LSF55 above ~250°C in air). The high oxygen ion conductivity of this hypothetical rhombohedral LSF phase compared to other real-world LSF compositions (i.e. those undergoing the phase transitions shown in Figure 1), is consistent with $La_{0.4}Sr_{0.6}FeO_{3-\delta}$ being considered the best LSF composition for 800°C SOFC operation[45–50] because, as can be inferred here, $La_{0.4}Sr_{0.6}FeO_{3-\delta}$ is the highest Sr doping level that can be achieved (in order to maximize the mobile oxygen vacancy concentration) while still realizing the high oxygen diffusivity of the rhombohedral phase.

In contrast to stabilizing rhombohedral LSF for high temperature SOFC operation, Figure 8c shows that superior SOFC ionic conductivity could be achieved below ~575°C by determining how to stabilize cubic SFO above ~300°C (as shown in Figure 1, cubic SFO undergoes an oxygen-vacancy-ordering-induced phase transition at ~300°C). Due to its low oxygen vacancy formation energy, cubic SFO possesses the highest oxygen ionic conductivity of any phase in the LFO-SFO solid solution between 0 and 1000°C. Though it was previously shown by Das *et al.*[25] that orthorhombic SFO possesses the highest oxygen vacancy concentration within the 0 – 1000°C SOFC operating window in the air, due to its high oxygen migration barrier, it is not predicted to be the best candidate as an oxygen ion conductor. It is left as a challenge the research community of how to best stabilize cubic SFO, but recent progress in high-entropy perovskite oxides[51] might be a promising new platform to tune the oxygen vacancy formation and migration for improved oxygen conductivity while maintaining the homogeneous single solid-solution cubic phase.

IV.   CONCLUSION

In summary, here the oxygen vacancy migration pathways, transition state structures, and energy barriers were predicted for multiple $La_{1-x}Sr_xFeO_{3-\delta}$ phases using a DFT based CINEB method. The oxidation state changes on the nearby Fe atoms during oxygen migration were obtained using magnetic-moment-calibrated charge states to reveal the distribution of excess electrons left on the lattice by neutral oxygen vacancy formation (i.e. the polaron shape). In general, the progressively larger polaron sizes occurring with increasing oxygen nonstoichiometry, and/or decreasing La/Sr ratio, resulted in increasing oxygen vacancy formation energies and higher oxygen migration barriers. This was consistent with experimental results[43] showing that Sr-rich LSF and highly oxygen deficient compositions are more prone to oxygen-vacancy-ordering-induced phase transformations that reduce the mobile oxygen vacancy concentration, while Sr-poor and oxygen rich LSF compositions are structurally stable.

It was found that the oxygen vacancy migration barrier does not change with the oxygen non-stoichiometry in rhombohedral LSF55 (0.45 eV) or orthorhombic LFO (0.89 eV), due to their small oxygen vacancy polaron size. Due to its stronger oxygen vacancy interactions, SFO demonstrates an increasing oxygen vacancy migration barrier with each subsequent oxygen-vacancy-ordering-induced phase change [cubic E_m =0.58 eV < tetragonal E_m =0.62 eV < orthorhombic E_m =1.07 eV]. LSF55 also shows an increased oxygen vacancy migration barrier (0.45 vs. 0.70 eV) after transforming from a rhombohedral to cubic structure. Comparing all the phases and compositions of LSF, the overall effect of phase changes on the oxygen vacancy migration barrier is not as substantial (it differs by < ~0.7 eV) as it is on the oxygen vacancy formation energy (this differs by ~3 eV).

16

The computationally predicted ionic conductivity showed that rhombohedral LSF55 has a higher 800°C ionic conductivity than cubic LSF55. However, cubic SFO is promising at low temperature, as it has the highest ionic conductivity of any other phase until its cubic to tetragonal phase transition. This work also suggests that ionic conductivity values even larger than "state-of-the-art" rhombohedral $La_{0.6}Sr_{0.4}FeO_{3-\delta}$ may be possible for low to intermediate temperature (~300-600°C) SOFCs by devising a way to extend the cubic SFO stability field to these higher temperatures.

Acknowledgments

REFERENCES

(1) Stefanik, T. S.; Tuller, H. L. Ceria-Based Gas Sensors. *J. Eur. Ceram. Soc.* **2001**, *21* (10–11), 1967–1970. https://doi.org/10.1016/S0955-2219(01)00152-2.
(2) Shao, Z. Investigation of the Permeation Behavior and Stability of a $Ba_{0.5}Sr_{0.5}Co_{0.8}Fe_{0.2}O_{3-\delta}$ Oxygen Membrane. *J. Membr. Sci.* **2000**, *172* (1–2), 177–188. https://doi.org/10.1016/S0376-7388(00)00337-9.
(3) Trovarelli, A. Catalytic Properties of Ceria and CeO_2 -Containing Materials. *Catal. Rev.* **1996**, *38* (4), 439–520. https://doi.org/10.1080/01614949608006464.
(4) Skinner, S. J. Recent Advances in Perovskite-Type Materials for Solid Oxide Fuel Cell Cathodes. *Int. J. Inorg. Mater.* **2001**, *3* (2), 113–121. https://doi.org/10.1016/S1466-6049(01)00004-6.

(5)   Jensen, S. H.; Larsen, P. H.; Mogensen, M. Hydrogen and Synthetic Fuel Production from Renewable Energy Sources. *Int. J. Hydrog. Energy* **2007**, *32* (15), 3253–3257. https://doi.org/10.1016/j.ijhydene.2007.04.042.

(6)   Yang, J. J.; Pickett, M. D.; Li, X.; Ohlberg, D. A. A.; Stewart, D. R.; Williams, R. S. Memristive Switching Mechanism for Metal/Oxide/Metal Nanodevices. *Nat. Nanotechnol.* **2008**, *3* (7), 429–433. https://doi.org/10.1038/nnano.2008.160.

(7)   Klingler, M.; Chu, W. F.; Weppner, W. Electrochromism by Polarization of Semiconducting Ionic Materials. *Ionics* **1995**, *1* (3), 251–256. https://doi.org/10.1007/BF02426026.

(8)   Mogensen, M.; Nigel, S.; Geoff, T. Physical, Chemical and Electrochemical Properties of Pure and Doped Ceria. *Solid State Ion.* **2000**, *129* (1–4), 63–94. https://doi.org/10.1016/S0167-2738(99)00318-5.

(9)   Xu, S.; Jacobs, R.; Morgan, D. Factors Controlling Oxygen Interstitial Diffusion in the Ruddlesden–Popper Oxide $La_{2-x}Sr_xNiO_{4+\delta}$. *Chem. Mater.* **2018**, *30* (20), 7166–7177. https://doi.org/10.1021/acs.chemmater.8b03146.

(10)   Burriel, M.; Peña-Martínez, J.; Chater, R. J.; Fearn, S.; Berenov, A. V.; Skinner, S. J.; Kilner, J. A. Anisotropic Oxygen Ion Diffusion in Layered $PrBaCo_2O_{5+\delta}$. *Chem. Mater.* **2012**, *24* (3), 613–621. https://doi.org/10.1021/cm203502s.

(11)   Jiang, S. P. Development of Lanthanum Strontium Cobalt Ferrite Perovskite Electrodes of Solid Oxide Fuel Cells – A Review. *Int. J. Hydrog. Energy* **2019**, *44* (14), 7448–7493. https://doi.org/10.1016/j.ijhydene.2019.01.212.

(12)   Mizusaki, J.; Sasamoto, T.; Cannon, W. R.; Bowen, H. K. Electronic Conductivity, Seebeck Coefficient, and Defect Structure of $La_{1-x}Sr_xFeO_3$ (x=0.l, 0.25). *J. Am. Ceram. Soc.* **1983**, *66* (4), 247–252. https://doi.org/10.1111/j.1151-2916.1983.tb15707.x.

(13)   Kuklja, M. M.; Kotomin, E. A.; Merkle, R.; Mastrikov, Yu. A.; Maier, J. Combined Theoretical and Experimental Analysis of Processes Determining Cathode Performance in Solid Oxide Fuel Cells. *Phys. Chem. Chem. Phys.* **2013**, *15* (15), 5443. https://doi.org/10.1039/c3cp44363a.

(14)   Ritzmann, A. M.; Muñoz-García, A. B.; Pavone, M.; Keith, J. A.; Carter, E. A. Ab Initio DFT+U Analysis of Oxygen Vacancy Formation and Migration in $La_{1-x}Sr_xFeO_{3-\delta}$ = 0, 0.25, 0.50). *Chem. Mater.* **2013**, *25* (15), 3011–3019. https://doi.org/10.1021/cm401052w.

(15)   Ren, Y.; Küngas, R.; Gorte, R. J.; Deng, C. The Effect of A-Site Cation (Ln=La, Pr, Sm) on the Crystal Structure, Conductivity and Oxygen Reduction Properties of Sr-Doped Ferrite Perovskites. *Solid State Ion.* **2012**, *212*, 47–54. https://doi.org/10.1016/j.ssi.2012.02.028.

(16)   Cassir, M.; Gourba, E. Reduction in the Operating Temperature of Solid Oxide Fuel Cells— Potential Use in Transport Applications. *Ann. Chim. Sci. Matér.* **2001**, *26* (4), 49–58.

(17)   Steele, B. C. H.; Heinzel, A. Materials for Fuel-Cell Technologies. *Nature* **2001**, *414* (6861), 345–352. https://doi.org/10.1038/35104620.

(18)   Dogdibegovic, E.; Wang, R.; Lau, G. Y.; Tucker, M. C. High Performance Metal-Supported Solid Oxide Fuel Cells with Infiltrated Electrodes. *J. Power Sources* **2019**, *410–411*, 91–98. https://doi.org/10.1016/j.jpowsour.2018.11.004.

(19)   Das, T.; Nicholas, J. D.; Qi, Y. Long-Range Charge Transfer and Oxygen Vacancy Interactions in Strontium Ferrite. *J. Mater. Chem. A* **2017**, *5* (9), 4493–4506. https://doi.org/10.1039/C6TA10357J.

(20) Lee, Y.-L.; Morgan, D. Ab Initio and Empirical Defect Modeling of LaMnO$_{3\pm\delta}$ for Solid Oxide Fuel Cell Cathodes. *Phys Chem Chem Phys* **2012**, *14* (1), 290–302. https://doi.org/10.1039/C1CP22380A.

(21) Kuklja, M. M.; Mastrikov, Y. A.; Jansang, B.; Kotomin, E. A. The Intrinsic Defects, Disordering, and Structural Stability of Ba$_x$Sr$_{1-x}$Co$_y$Fe$_{1-y}$O$_{3-\delta}$ Perovskite Solid Solutions. *J. Phys. Chem. C* **2012**, *116* (35), 18605–18611. https://doi.org/10.1021/jp304055s.

(22) Maier, J. *Physical Chemistry of Ionic Materials: Ions and Electrons in Solids*; Wiley: Chichester ; Hoboken, NJ, 2004.

(23) Pan, J.; Cheng, Y.-T.; Qi, Y. General Method to Predict Voltage-Dependent Ionic Conduction in a Solid Electrolyte Coating on Electrodes. *Phys. Rev. B* **2015**, *91* (13), 134116. https://doi.org/10.1103/PhysRevB.91.134116.

(24) Chroneos, A.; Yildiz, B.; Tarancón, A.; Parfitt, D.; Kilner, J. A. Oxygen Diffusion in Solid Oxide Fuel Cell Cathode and Electrolyte Materials: Mechanistic Insights from Atomistic Simulations. *Energy Environ. Sci.* **2011**, *4* (8), 2774. https://doi.org/10.1039/c0ee00717j.

(25) Das, T.; Nicholas, J. D.; Qi, Y. Polaron Size and Shape Effects on Oxygen Vacancy Interactions in Lanthanum Strontium Ferrite. *J. Mater. Chem. A* **2017**. https://doi.org/10.1039/C7TA06948K.

(26) Ishigaki, T.; Yamauchi, S.; Kishio, K.; Mizusaki, J.; Fueki, K. Diffusion of Oxide Ion Vacancies in Perovskite-Type Oxides. *J. Solid State Chem.* **1988**, *73* (1), 179–187. https://doi.org/10.1016/0022-4596(88)90067-9.

(27) De Souza, R. A.; Kilner, J. A. Oxygen Transport in La$_{1-x}$Sr$_x$Mn$_{1-y}$Co$_y$O$_{3\pm\delta}$ Perovskites: Part I. Oxygen Tracer Diffusion. *Solid State Ion.* **1998**, *106* (3–4), 175–187. https://doi.org/10.1016/S0167-2738(97)00499-2.

(28) Berenov, A. V.; Atkinson, A.; Kilner, J. A.; Bucher, E.; Sitte, W. Oxygen Tracer Diffusion and Surface Exchange Kinetics in La$_{0.6}$Sr$_{0.4}$CoO$_{3-\delta}$. *Solid State Ion.* **2010**, *181* (17–18), 819–826. https://doi.org/10.1016/j.ssi.2010.04.031.

(29) Mastrikov, Y. A.; Merkle, R.; Kotomin, E. A.; Kuklja, M. M.; Maier, J. Formation and Migration of Oxygen Vacancies in La$_{1-x}$Sr$_x$Co$_{1-y}$Fe$_y$O$_{3-\delta}$ Perovskites: Insight from Ab Initio Calculations and Comparison with Ba$_{1-x}$Sr$_x$Co$_{1-y}$Fe$_y$O$_{3-\delta}$. *Phys Chem Chem Phys* **2013**, *15* (3), 911–918. https://doi.org/10.1039/C2CP43557H.

(30) Mayeshiba, T. T.; Morgan, D. D. Factors Controlling Oxygen Migration Barriers in Perovskites. *Solid State Ion.* **2016**, *296*, 71–77. https://doi.org/10.1016/j.ssi.2016.09.007.

(31) Yoo, J. Determination of the Equilibrium Oxygen Non-Stoichiometry and the Electrical Conductivity of La$_{0.5}$Sr$_{0.5}$FeO$_{3-x}$. *Solid State Ion.* **2004**, *175* (1–4), 55–58. https://doi.org/10.1016/j.ssi.2004.09.026.

(32) Takeda, Y.; Kanno, K.; Takada, T.; Yamamoto, O.; Takano, M.; Nakayama, N.; Bando, Y. Phase Relation in the Oxygen Nonstoichiometric System, SrFeO$_x$ (2.5 ≤ x ≤ 3.0). *J. Solid State Chem.* **1986**, *63* (2), 237–249. https://doi.org/10.1016/0022-4596(86)90174-X.

(33) Hombo, J.; Matsumoto, Y.; Kawano, T. Electrical Conductivities of SrFeO$_{3-\delta}$ and BaFeO$_{3-\delta}$ Perovskites. *J. Solid State Chem.* **1990**, *84* (1), 138–143. https://doi.org/10.1016/0022-4596(90)90192-Z.

(34) Kharton, V.; Kovalevsky, A.; Tsipis, E.; Viskup, A.; Naumovich, E.; Jurado, J.; Frade, J. Mixed Conductivity and Stability of A-Site-Deficient Sr(Fe,Ti)O$_{3-\delta}$ Perovskites. *J. Solid State Electrochem.* **2002**, *7* (1), 30–36. https://doi.org/10.1007/s10008-002-0286-3.

(35) Lee, C.-W.; Behera, R. K.; Wachsman, E. D.; Phillpot, S. R.; Sinnott, S. B. Stoichiometry of the LaFeO$_3$ (010) Surface Determined from First-Principles and Thermodynamic

Calculations. *Phys. Rev. B* **2011**, *83* (11), 115418. https://doi.org/10.1103/PhysRevB.83.115418.

(36) Greg Mills, K. W. J. Nudged Elastic Band Method for Finding Minimum Energy Paths of Transitions. **1998**.

(37) Henkelman, G.; Uberuaga, B. P.; Jónsson, H. A Climbing Image Nudged Elastic Band Method for Finding Saddle Points and Minimum Energy Paths. *J. Chem. Phys.* **2000**, *113* (22), 9901–9904. https://doi.org/10.1063/1.1329672.

(38) Sheppard, D.; Terrell, R.; Henkelman, G. Optimization Methods for Finding Minimum Energy Paths. *J. Chem. Phys.* **2008**, *128* (13), 134106. https://doi.org/10.1063/1.2841941.

(39) Tucker, M. C. Progress in Metal-Supported Solid Oxide Fuel Cells: A Review. *J. Power Sources* **2010**, *195* (15), 4570–4582. https://doi.org/10.1016/j.jpowsour.2010.02.035.

(40) Mantina, M.; Wang, Y.; Chen, L. Q.; Liu, Z. K.; Wolverton, C. First Principles Impurity Diffusion Coefficients. *Acta Mater.* **2009**, *57* (14), 4102–4108. https://doi.org/10.1016/j.actamat.2009.05.006.

(41) Wærnhus, I.; Grande, T.; Wiik, K. Surface Exchange of Oxygen in $La_{1-x}Sr_xFeO_{3-\delta}$ (x = 0, 0.1). *Top. Catal.* **2011**, *54* (13–15), 1009–1015. https://doi.org/10.1007/s11244-011-9712-z.

(42) Das, T.; Nicholas, J. D.; Qi, Y. First-Principles Studies of Oxygen Vacancy Interactions and Their Impact on Oxygen Migration in Lanthanum Strontium Ferrite. *ECS Trans.* **2017**, *78* (1), 2807–2814. https://doi.org/10.1149/07801.2807ecst.

(43) Fossdal, A.; Menon, M.; Wærnhus, I.; Wiik, K.; Einarsrud, M.-A.; Grande, T. Crystal Structure and Thermal Expansion of $La_{1-x}Sr_xFeO_{3-\delta}$ Materials. *J. Am. Ceram. Soc.* **2004**, *87* (10), 1952–1958. https://doi.org/10.1111/j.1151-2916.2004.tb06346.x.

(44) Patrakeev, M. V.; Bahteeva, J. A.; Mitberg, E. B.; Leonidov, I. A.; Kozhevnikov, V. L.; Poeppelmeier, K. R. Electron/Hole and Ion Transport in $La_{1-x}Sr_xFeO_{3-\delta}$. *J. Solid State Chem.* **2003**, *172* (1), 219–231. https://doi.org/10.1016/S0022-4596(03)00040-9.

(45) Yang, Q.; Burye, T. E.; Lunt, R. R.; Nicholas, J. D. In Situ Oxygen Surface Exchange Coefficient Measurements on Lanthanum Strontium Ferrite Thin Films via the Curvature Relaxation Method. *Solid State Ion.* **2013**, *249–250* (0), 123–128. https://doi.org/10.1016/j.ssi.2013.07.025.

(46) ten Elshof, J. E.; Lankhorst, M. H. R.; Bouwmeester, H. J. M. Chemical Diffusion and Oxygen Exchange of $La_{0.6}Sr_{0.4}Co_{0.6}Fe_{0.4}O_{3-\delta}$. *Solid State Ion.* **1997**, *99* (1–2), 15–22. https://doi.org/10.1016/S0167-2738(97)00263-4.

(47) Mosleh, M.; Søgaard, M.; Hendriksen, P. V. Kinetics and Mechanisms of Oxygen Surface Exchange on $La_{0.6}Sr_{0.4}FeO_{3-\delta}$ Thin Films. *J. Electrochem. Soc.* **2009**, *156* (4), B441–B457. https://doi.org/10.1149/1.3062941.

(48) Søgaard, M.; Vang Hendriksen, P.; Mogensen, M. Oxygen Nonstoichiometry and Transport Properties of Strontium Substituted Lanthanum Ferrite. *J. Solid State Chem.* **2007**, *180* (4), 1489–1503. https://doi.org/10.1016/j.jssc.2007.02.012.

(49) Søgaard, M.; Bieberle-Hütter, A.; Hendriksen, P. V.; Mogensen, M.; Tuller, H. L. Oxygen Incorporation in Porous Thin Films of Strontium Doped Lanthanum Ferrite. *J. Electroceramics* **2011**, *27* (3–4), 134–142. https://doi.org/10.1007/s10832-011-9658-3.

(50) Burye, T. E.; Tang, H.; Nicholas, J. D. The Effect of Precursor Solution Desiccation or Nano-Ceria Pre-Infiltration on Various $La_{0.6}Sr_{0.4}Fe_yCo_{1-y}O_{3-x}$ Infiltrate Compositions. *J. Electrochem. Soc.* **2016**, *163* (9), F1017–F1022. https://doi.org/10.1149/2.0431609jes.

(51) Jiang, S.; Hu, T.; Gild, J.; Zhou, N.; Nie, J.; Qin, M.; Harrington, T.; Vecchio, K.; Luo, J. A New Class of High-Entropy Perovskite Oxides. *Scr. Mater.* **2018**, *142*, 116–120. https://doi.org/10.1016/j.scriptamat.2017.08.040.

Table 1 Structure details for the DFT vacancy calculations and the DFT computed vacancy formation energy E_f (at 0K) and migration energy barrier E_b.

| Phase	Unit Cell Lattice Parameters (Å)			Supercell cell with vacancy				
	a	b	c	δ	# of atoms	Cell Length (Å)	E_f (eV)	E_b (eV)
LaFeO₃ (Orthorhombic)	5.67	7.92	5.58	0.06	$La_{16}Fe_{16}O_{47}$	11.34×7.92×11.16	3.54	0.89
				0.25	$La_4Fe_4O_{11}$	5.67×7.92×5.58	3.61	0.88
La₀.₅Sr₀.₅FeO₃ (Rhombohedral)	5.51	-	-	0.04	$La_{12}Sr_{12}Fe_{24}O_{71}$	11.13×11.13×13.45	1.62	0.45
				0.17	$La_3Sr_3Fe_6O_{17}$	5.56×5.56×13.45	1.83	0.44
La₀.₅Sr₀.₅FeO₃ (Cubic)	5.53	-	-	0.13	$La_4Sr_4Fe_8O_{23}$	11.05×11.05×11.05	1.45	0.70
SrFeO₃ (Cubic)	3.88	-	-	0.04	$Sr_{24}Fe_{24}O_{71}$	10.97×10.97×11.64	0.39	0.58
				0.12	$Sr_8Fe_8O_{23}$	7.76×7.76×11.64	0.71	0.62
				0.5	$Sr_2Fe_2O_5$	5.49×5.49×3.88	1.45	1.07
SrFeO₂.₈₇₅ (Tetragonal)	11.03	-	7.76	0.188	$Sr_{16}Fe_{16}O_{45}$	11.03×11.03×7.76	0.92	0.71
SrFeO₂.₇₅ (Orthorhombic)	11.09	7.78	5.52	0.312	$Sr_{16}Fe_{16}O_{43}$	7.78×11.09×11.04	1.25	1.17
SrFeO₂.₅ (Brownmillerite)	5.58	15.70	5.77	0.625	$Sr_8Fe_8O_{19}$	5.58×15.70×5.77	3.00	-
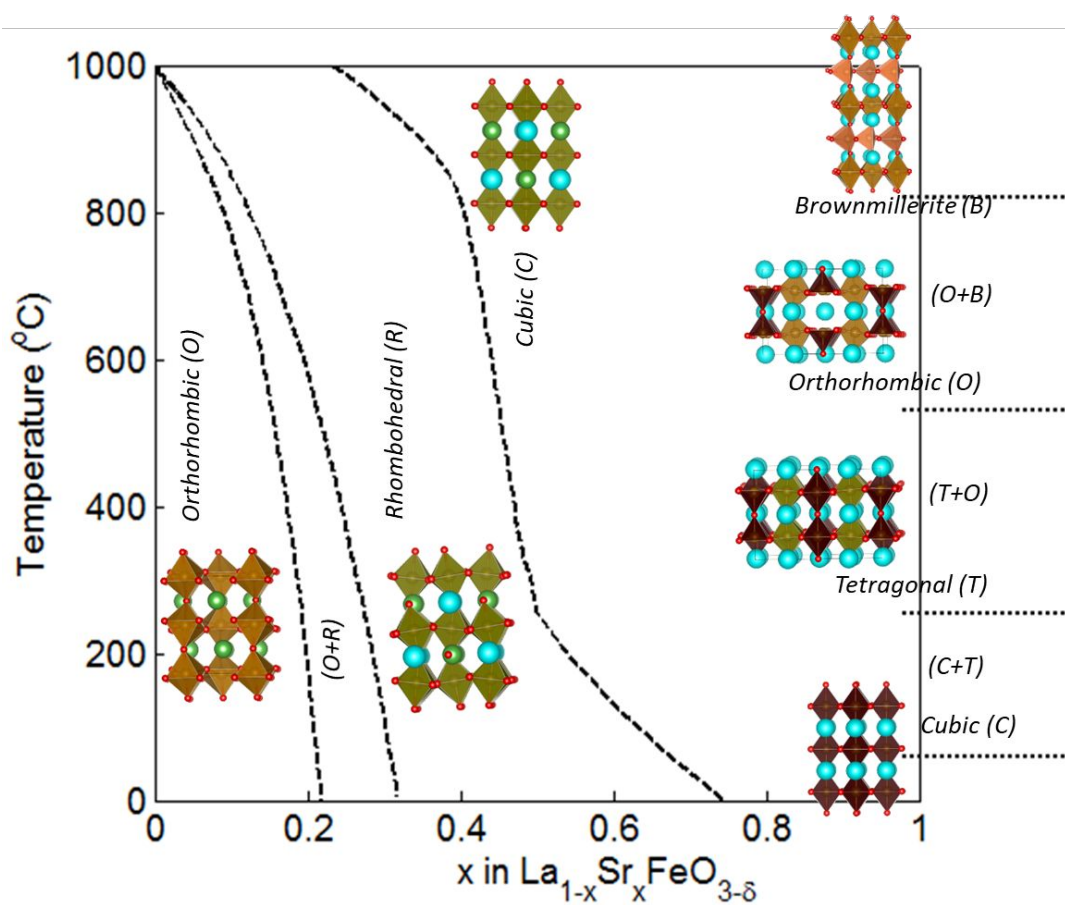
Figure 1. (Color online) Experimentally determined LSF phase boundaries with varying La/Sr ratio and temperature in air. The lattice structure of the corresponding phases are shown for reference.[25]
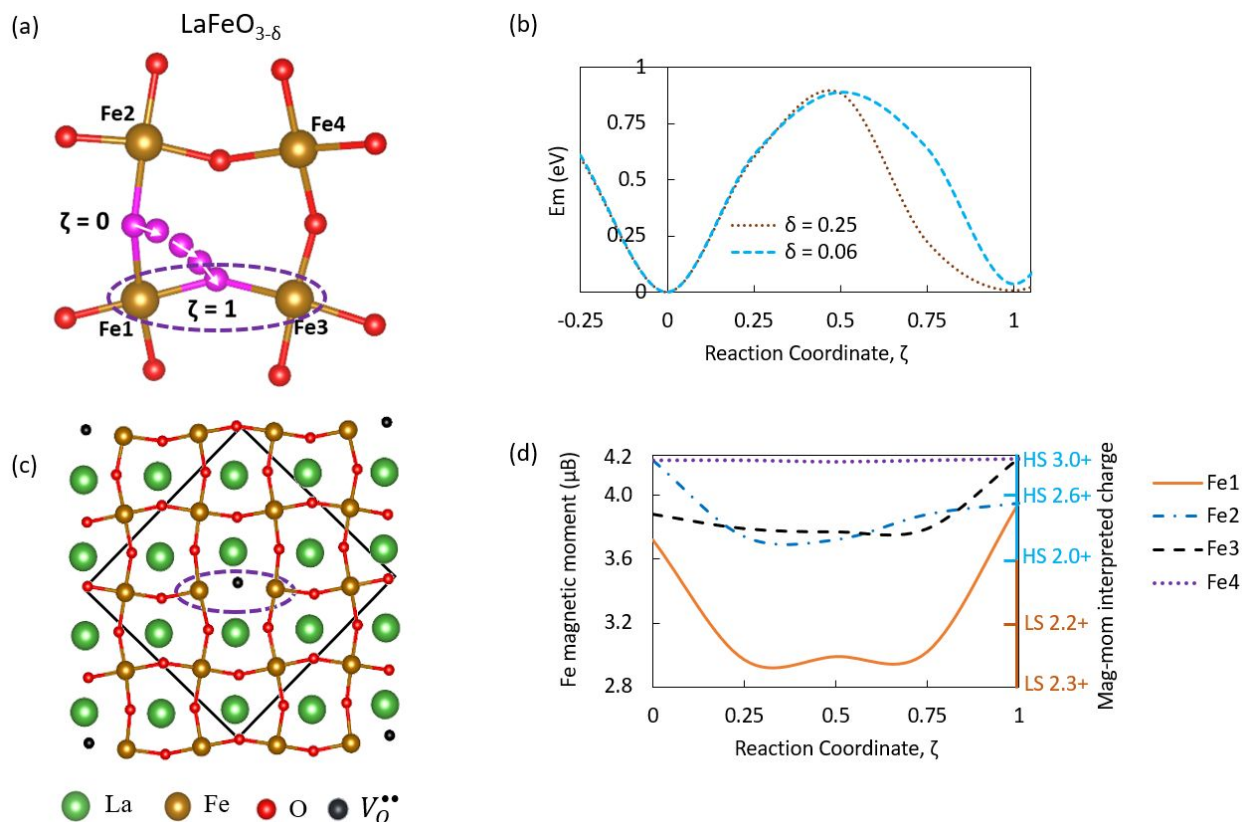
Figure 2. (Color online) Oxygen migration in LaFeO$_{3-\delta}$. The pink atoms in (a) highlight the oxygen migration pathway (with the lattice pictured at the transition state), (b) shows the oxygen migration barrier along this path for two different δ, (c) shows a cross-section of the oxygen vacancy (the black dot) migration plane, and (d) shows the magnetic moment change on the neighboring Fe atoms during oxygen vacancy migration along the path shown in (a). The purple dashed line in (c) signifies the polaron volume (i.e. the long-range change transfer area due to the presence of the oxygen vacancy). The calculated magnetic moment and the interpreted change state (HS and LS denote high spin and low spin, respectively) change on the oxygen-vacancy-neighboring Fe atoms shown in (d) results from charge transfer during oxygen ion migration. Note, the La atoms are hidden in part (a) so the migration pathways can be more easily seen.
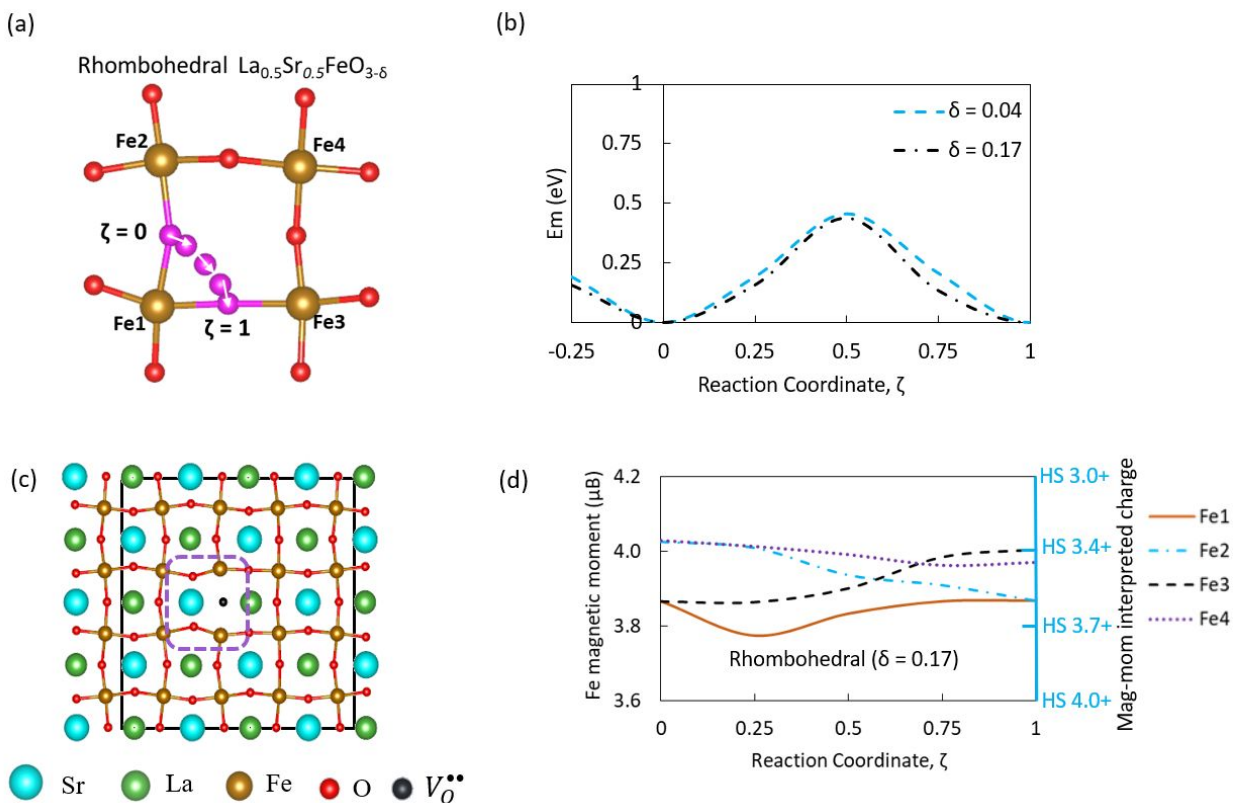
Figure 3. (Color online) Oxygen migration in Rhombohedral $(LaSr)FeO_{3-\delta}$ for δ =0.04 and δ =0.17. The pink atoms in (a) highlight the oxygen migration pathway (with the lattice pictured at the transition state), (b) shows the oxygen migration barrier along this path, (c) shows a cross-section of the oxygen vacancy (the black dot) migration plane, and (d) shows the magnetic moment change on the neighboring Fe atoms during oxygen vacancy migration along the path shown in (a). The purple dashed line in (c) signifies the polaron volume (i.e. the long-range change transfer area due to the presence of the oxygen vacancy). The calculated magnetic moment and the interpreted change state (HS denotes high spin) on the oxygen-vacancy-neighboring Fe atoms shown in (d) results from charge transfer during oxygen ion migration. Note, the La and Sr atoms are hidden in part (a) so the migration pathways can be more easily seen.

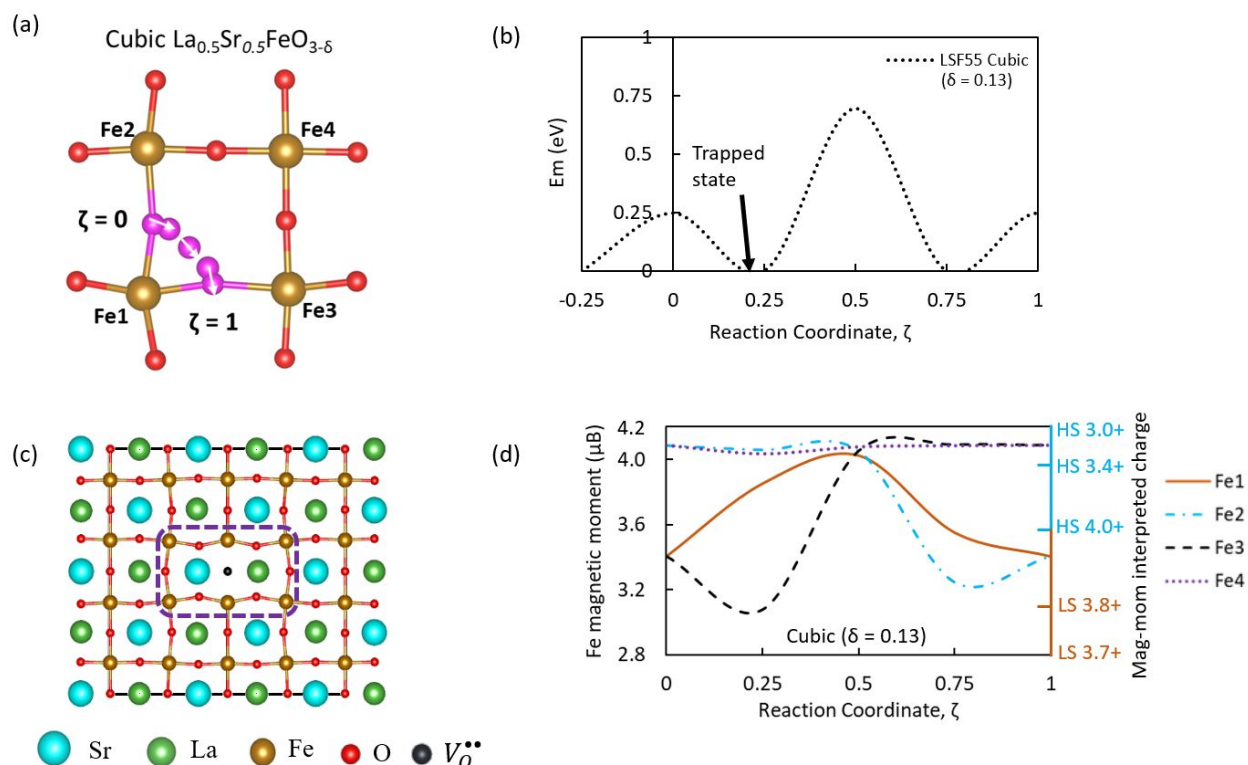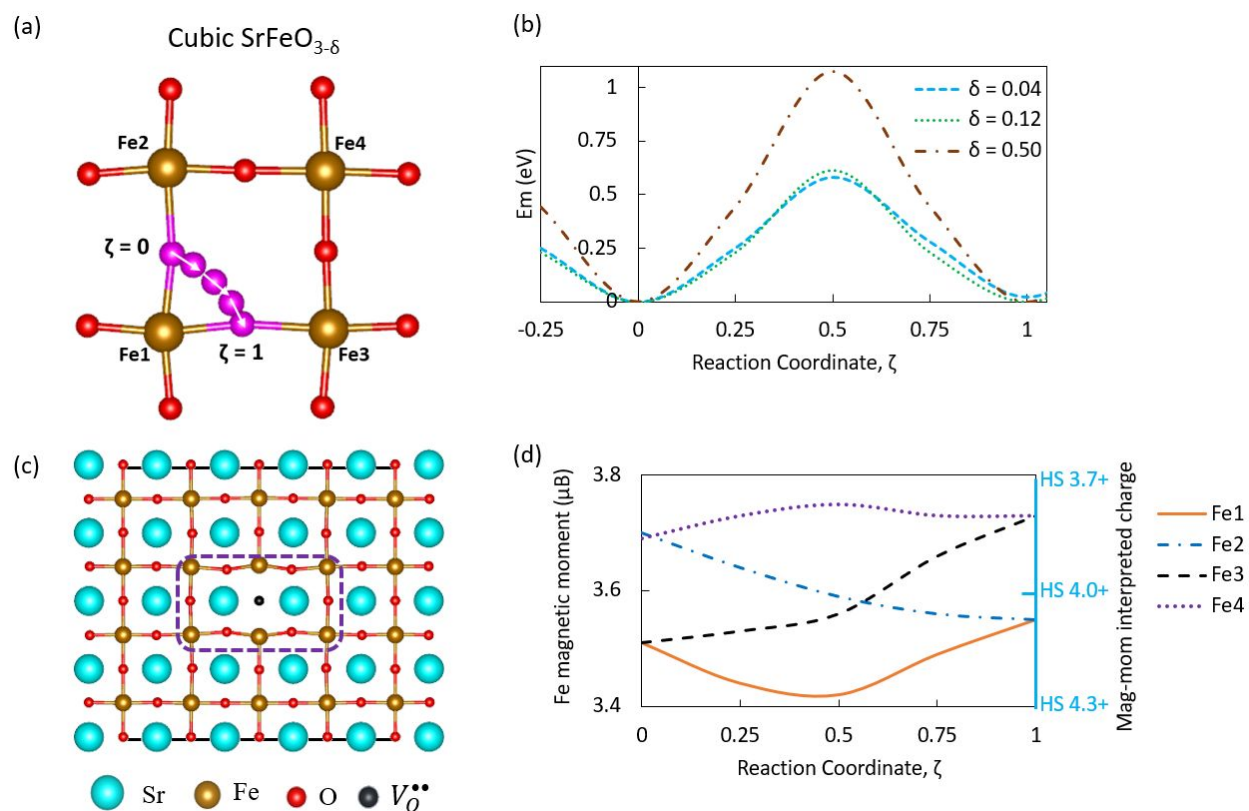**Figure 4.** (Color online) Oxygen migration in cubic (LaSr)FeO$_{3-\delta}$ for δ =0.13. The pink atoms in (a) highlight the oxygen migration pathway (with the lattice pictured at the transition state), (b) shows the oxygen migration barrier along this path, (c) shows a cross-section of the oxygen vacancy (the black dot) migration plane, and (d) shows the magnetic moment change on the neighboring Fe atoms during oxygen vacancy migration along the path shown in (a). The purple dashed line in (c) signifies the polaron volume (i.e. the long-range change transfer area due to the presence of the oxygen vacancy). The calculated magnetic moment and the interpreted change state (HS and LS denote high spin and low spin, respectively) on the oxygen-vacancy-neighboring Fe atoms shown in (d) results from charge transfer during oxygen ion migration. Note, the La and Sr atoms are hidden in part (a) so the migration pathways can be more easily seen.

Figure 5. (Color online) Oxygen migration in cubic $SrFeO_{3-\delta}$. Here, (a) highlights the oxygen migration pathway (with the lattice pictured at the transition state) in cubic $SrFeO_{3-\delta}$ at δ =0.04, (b) shows the oxygen migration barrier along this path for three different δ, (c) shows a cross-section of the oxygen vacancy migration plane in cubic $SrFeO_{3-\delta}$ for δ =0.04, and (d) shows the magnetic moment change on the neighboring Fe atoms during oxygen vacancy migration along the path shown in (a). The purple dashed line in (c) signifies the polaron volume (i.e. the long range change transfer area due to the presence of the oxygen vacancy). The calculated magnetic moment and the interpreted change state (HS denotes high spin) on the oxygen-vacancy-neighboring Fe atoms shown in (d) results from charge transfer during oxygen ion migration cubic $SrFeO_{3-\delta}$ at δ =0.04. Note, the Sr atoms are hidden in part (a) so the migration pathways can be more easily seen.

Tetragonal SrFeO$_{3-\delta}$

(a)

4c →16k →8h →16k →4c   4c →16k →16m →16k →4c   4c →16k →4c

(b)

(c)

Sr   Fe   O $V_O^{\bullet\bullet}$

(δ = 0.19)

$\vec{a}$
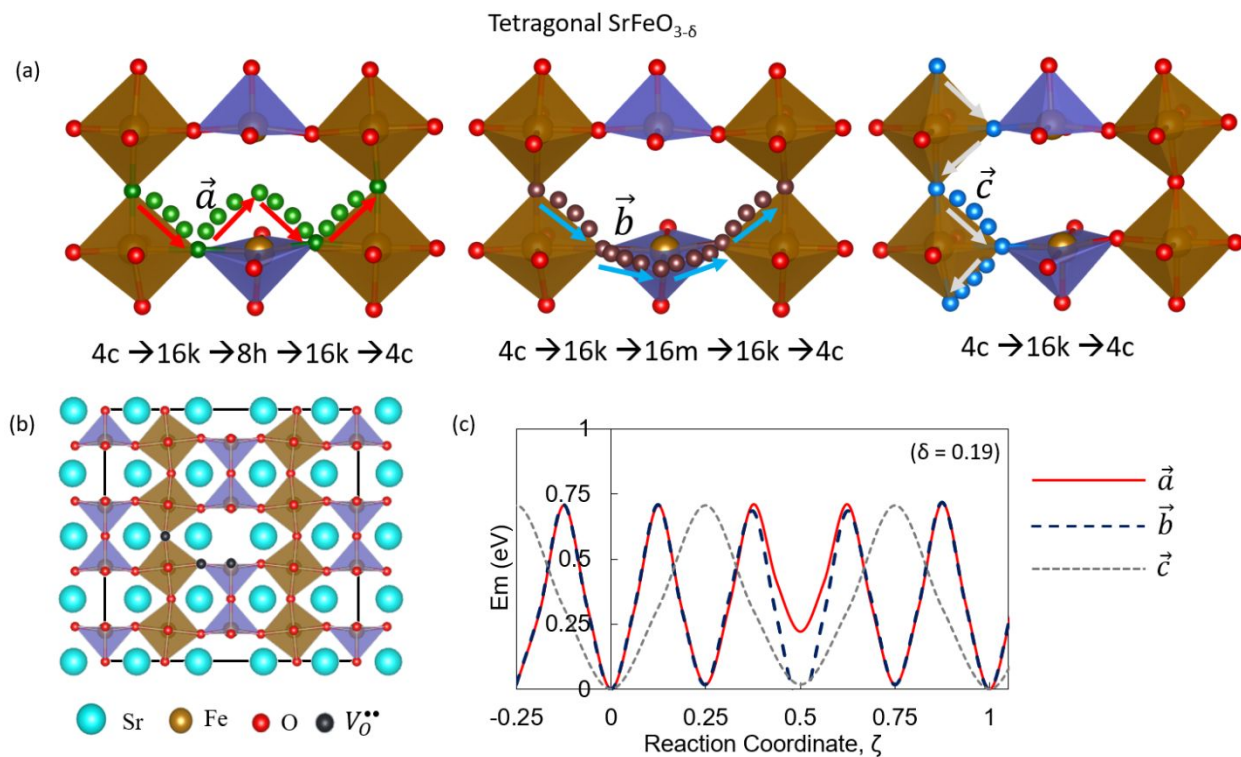$\vec{b}$
$\vec{c}$

Em (eV)

Reaction Coordinate, ζ

Figure 6. (Color online) Oxygen migration in tetragonal SrFeO$_{3-\delta}$ with $\delta = 0.188$ and $\delta^0 = 0.125$. Only Fe (brown) and O (red) atoms are shown in the lattice for ease of visibility. (a) The green, dark brown, and dark blue atoms highlight three different oxygen migration pathways that labeled by different Wyckoff positions. Path $\vec{a}$ follows 4c → 16k → 8h → 16k → 4c; Path $\vec{b}$ follows 4c → 16k → 16m → 16k → 4c; and Path $\vec{c}$ follows 4c → 16k → 4c (b) shows a cross-section of the oxygen vacancy migration plane and (c) shows the oxygen migration barriers along these pathways.
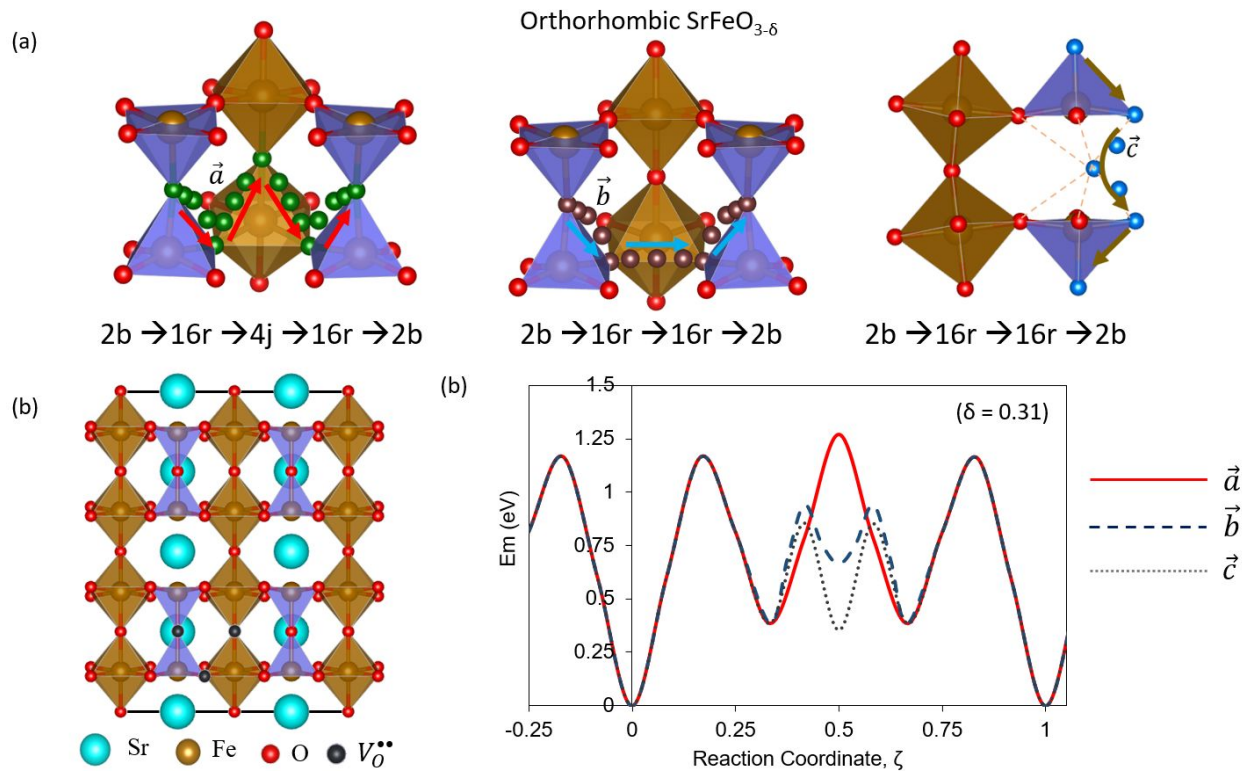
Figure 7. (Color online) Oxygen migration in orthorhombic SrFeO$_{3-\delta}$ with for $\delta = 0.312$ and $\delta^0 = 0.250$. Only Fe (brown) and O (red) atoms are shown in the lattice for ease of visibility. (a) The green, dark brown, and dark blue atoms highlight three different oxygen migration pathways that labeled by different Wyckoff positions. Path $\vec{a}$ follows 2b → 16r → 16r → 2b; Path $\vec{b}$ follows 2b → 16r → 4j → 16r → 2b; and Path $\vec{c}$ follows 2b → 16r → 16r → 2b (b) shows a cross-section of the oxygen vacancy migration plane and (c) shows the oxygen migration barriers along these pathways.
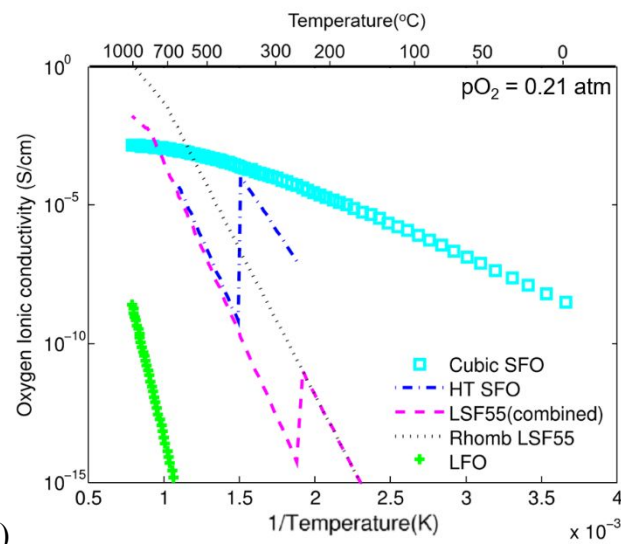
(a)

(b)

(c)

Submit to PCCP
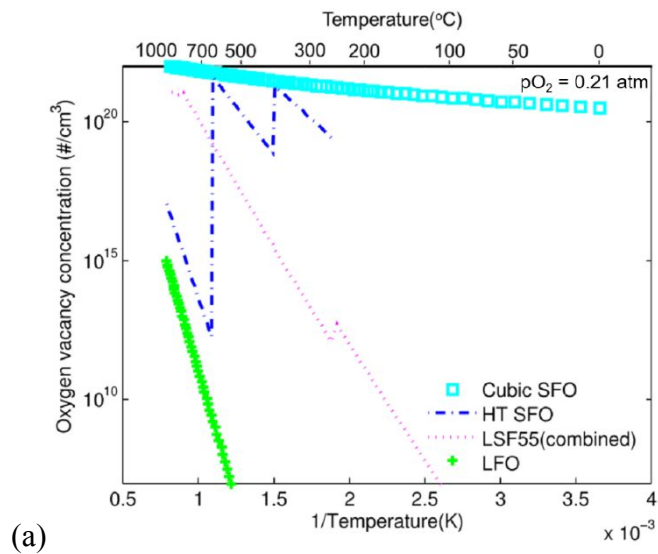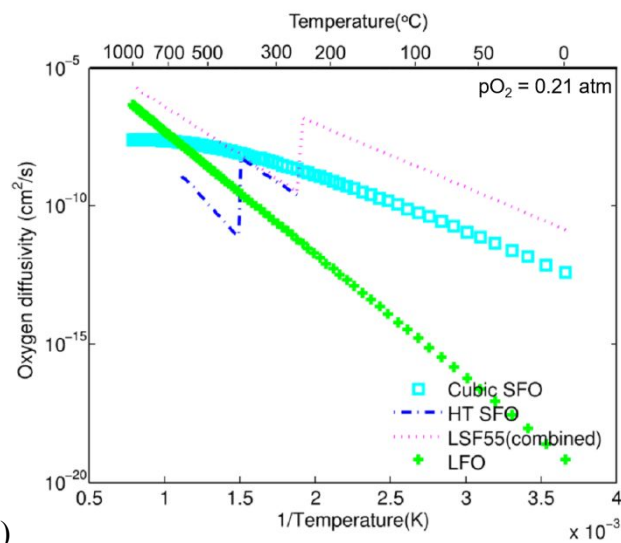
Figure 8. (Color online) The (a) mobile oxygen vacancy concentration, (b) oxygen vacancy diffusivity, and (c) oxygen vacancy conductivity in different LSF compositions as a function of temperature in air. 'Cubic SFO' represents cubic $SrFeO_{3-\delta}$. 'HT SFO' represents combined data for tetragonal, orthorhombic, and brownmillerite phases (note, due to a very low oxygen vacancy concentration, diffusivity and conductivity calculations were not performed for brownmillerite SFO). 'LSF55(combined)' represents LSF55 that experiences the rhombohedral to cubic phase change. 'Rhomb LSF55' represents real and hypothetical data for rhombohedral LSF55.